Bioactive Materials 25 (2023) 347–359

Contents lists available at ScienceDirect

Bioactive Materials

journal homepage: www.keaipublishing.com/en/journals/bioactive-materials

Stiffness-tuned and ROS-sensitive hydrogel incorporating complement C5a receptor antagonist modulates antibacterial activity of macrophages for periodontitis treatment

Ziqi Gan [a,1], Zecong Xiao [b,1,**], Zhen Zhang [a,1], Yang Li [a], Chao Liu [a], Xin Chen [a], Yuanbo Liu [a], Dongle Wu [a], Chufeng Liu [c,***], Xintao Shuai [b,*], Yang Cao [a,****]

[a] Hospital of Stomatology, Guangdong Provincial Key Laboratory of Stomatology, Guanghua School of Stomatology, Sun Yat-sen University, Guangzhou, 510055, China
[b] Nanomedicine Research Center, The Third Affiliated Hospital of Sun Yat-sen University, Guangzhou, 510630, China
[c] Stomatological Hospital, Southern Medical University, Guangzhou, 510260, China

ARTICLE INFO

Keywords:
Periodontitis treatment
Cell therapy
ROS-Responsive hydrogels
C5a receptor blockade
Mechanostimulation

ABSTRACT

Periodontitis is admittedly a microbe-driven intractable infectious disease, in which *Porphyromonas gingivalis* (*Pg*) plays a keystone role. *Pg* can selectively impair the antimicrobial responses of periodontal resident macrophages including their phagocytic and bactericidal activity without interfering their proinflammatory activity, which leads to microflora disturbance, destructive periodontal inflammation and alveolar bone loss eventually. Here, an injectable ROS-sensitive hydrogel is developed for releasing active bone marrow-derived macrophages (named *ex-situ* macrophages hereafter) and a complement C5a receptor antagonist (C5A) to the gingival crevice. Through appropriately tuning the hydrogel stiffness, the phagocytic activity of these macrophages is greatly enhanced, reaching an optimal performance at the elastic modulus of 106 kPa. Meanwhile, C5A avoids undesired C5a receptor activation by *Pg* to ensure the bacterial killing activity of both the *ex-situ* and *in-situ* macrophages. Besides, the ROS-sensitive hydrogels show another distinct feature of decreasing the ROS level in periodontal niche, which contributes to the alleviated periodontal inflammation and attenuated bone loss as well. This study highlights the potential of utilizing hydrogels with tailored biomechanical properties to remodel the functions of therapeutic cells, which is expected to find wide applications even beyond periodontitis treatment.

1. Introduction

Periodontitis is the sixth-most prevalent inflammatory disease worldwide characterized by inflamed gingiva and loss of tooth-supporting tissues, which afflicts more than 10% of adults and imparts a large socioeconomic burden [1]. Growing evidence reveals that periodontitis is heavily implicated in the periodontal microbial dysbiosis, in which *Porphyromonas gingivalis* (*Pg*) plays a keystone role [2,3]. As the most important activist in periodontal microbial community, *Pg* impairs the host immune surveillance to promote the fitness of the entire community and fuel the selective expansion of periodontitis-associated bacteria [4,5]. Therefore, a homeostatic commensal microbial community is shifted toward a disease-provoking one, which eventually initiates or aggravates periodontitis [6]. Moreover, uncontrolled *Pg* derived from the inflamed periodontal tissues may enter the bloodstream and relocate to other target organs [7]. It is thus not surprising to see an epidemiological link between periodontitis and several systemic diseases such as type-2 diabetes, cardiovascular disease, rheumatoid arthritis, Alzheimer disease, and some cancers [8,9]. Therefore, eliminating this keystone pathogen may be critical for treating periodontitis

Peer review under responsibility of KeAi Communications Co., Ltd.
* Corresponding author.
** Corresponding author.
*** Corresponding author.
**** Corresponding author. Hospital of Stomatology, Guangdong Provincial Key Laboratory of Stomatology, Guanghua School of Stomatology, Sun Yat-sen University, Guangzhou, 510055, China.
E-mail addresses: xiao92826@hotmail.com (Z. Xiao), xyzmmok@smu.edu.cn (C. Liu), shuaixt@mail.sysu.edu.cn (X. Shuai), caoyang@mail.sysu.edu.cn (Y. Cao).
[1] These authors contributed equally to this work.

https://doi.org/10.1016/j.bioactmat.2023.01.011
Received 17 October 2022; Received in revised form 7 January 2023; Accepted 12 January 2023

as well as reducing the risk of periodontitis-associated comorbidities.

Thus far, there are still many challenges to clear *Pg* from the infected periodontal tissues, mainly because *Pg* has developed multiple pathways to escape the clearance by host immune cells. Chief among them, *Pg* can largely interfere the antibacterial activity of the periodontal resident macrophages (*i.e., in-situ* macrophages) [10,11]. For example, *Pg* selectively downregulates the expression of CD14 [12], known as a receptor to identify "eat me" signals of pathogens [13], thereby impeding the macrophage-mediated phagocytosis. Even worse, the phagocytosed *Pg* may still survive for a long time *via* impairing the bactericidal activity of the macrophages [10]. Specifically, *Pg* secretes the virulence factors (HRgpA, RgpB) to stimulate excessive C5a production in an uncontrolled manner, which results in pathological activation of complement C5a receptor (C5aR) in the macrophages [14]. This *Pg*-triggered C5aR activation not only generates high amounts of cyclic adenosine monophosphate *via* a co-activation with Toll-like receptor 2 [15], but also suppresses Toll-like receptor 4-induced IL-12p70 production [14,16], both decreasing the nitric oxide (NO) production to increase *Pg* survival [17]. Given the fact that *Pg* can disable the *in-situ* resident macrophages, delivering *ex-situ* macrophages whose C5aR is shut off and phagocytic capacity is enhanced into the infected periodontal sites may represent a highly effective strategy against *Pg*.

Cell-based therapy has shown great promise in regenerative medicine and cancer immunotherapy [18]. However, this approach remains unexploited in treating periodontitis. Hydrogels have long been employed as ideal cell carriers since they can support long-term cell survival and retention required in local therapeutic means, and present mechanical and functional tunability [19,20]. In particular, introducing stimulation-sensitive groups into the hydrogel network can make it responsive to the disease-specific microenvironments featuring hypoxia, low pH, enriched reactive oxygen species (ROS), *etc.* [21], thus achieving a controlled cell release in the focal sites [22]. More importantly, the mechanobiological communication between cells and their three-dimensional extracellular matrices has a considerable impact on the functions of therapeutic cells [23,24]. Tuning the mechanical properties of hydrogels such as stiffness can alter the cell morphology, differentiation and metabolism so as to achieve desirable therapeutic effects [25]. During the process of cell-matrix interaction, actin as a major component of cytoskeleton is mainly responsible for probing and transducing the external mechanical signals into the intracellular biochemical signals [23,26]. Meanwhile, actin also plays a pivotal role in the phagocytosis of pathogens by macrophages as it participates in multiple key stages including cytoskeletal remodeling, membrane protrusion and pathogen engulfment [27]. These facts enlightened us to explore whether the phagocytic activity of macrophages could be substantially boosted through tuning the mechanical properties of hydrogels in order to affect the shared effector, actin cytoskeleton.

Herein, an injectable ROS-sensitive cross-linked poly (vinyl alcohol) (PVA) hydrogel was prepared for co-delivering the bone marrow-derived macrophages (*i.e., ex-situ* macrophages) and a C5aR antagonist (C5A, using a commercially available product PMX53) into the gingival crevice (Fig. 1). The hydrogel stiffness was adjusted by altering the crosslinking density, which was expected to boost the phagocytic activity of the encapsulated macrophages. The incorporated C5A was

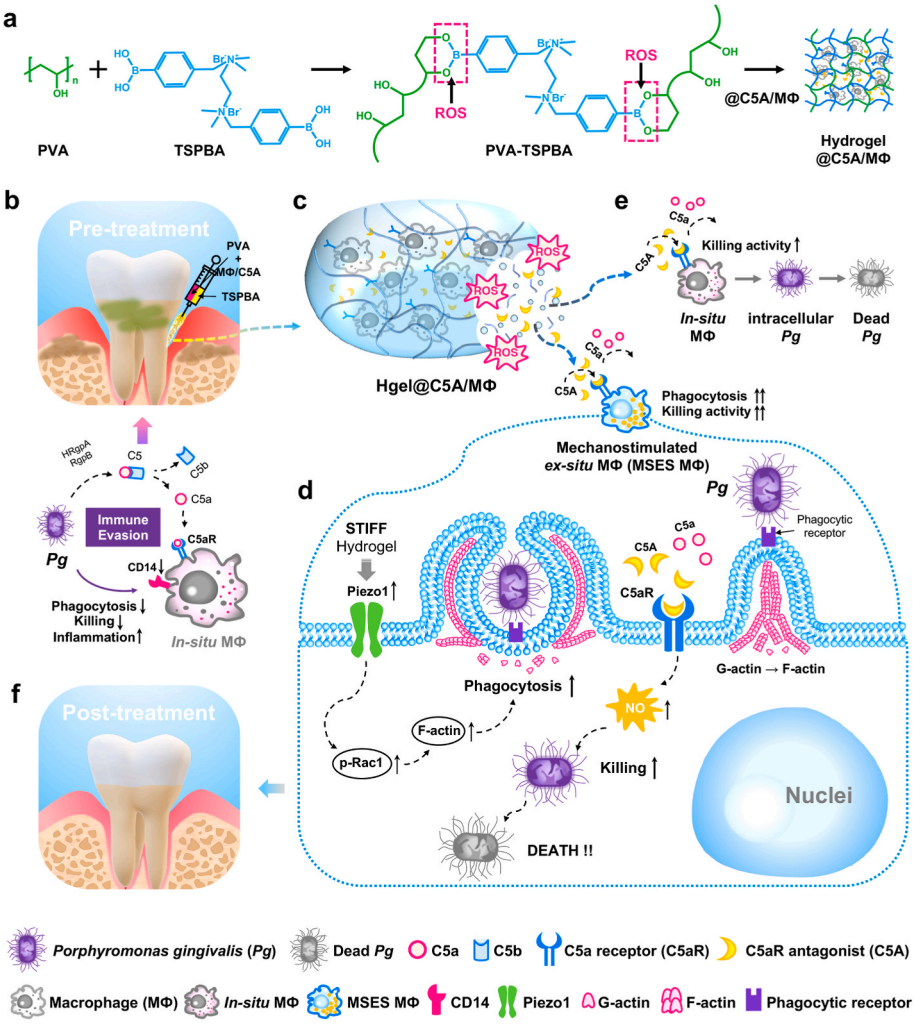

Fig. 1. Schematic illustration of mechanism how the high modulus ROS-sensitive hydrogel encapsulating macrophages and C5aR antagonists (Hgel@C5A/MΦ) treats periodontitis. (a) Diagram of the preparation of the PVA-TSPBA hydrogel. (b) Illustration of the administration of Hgel@C5A/MΦ and the mechanism of *Pg* immune evasion. (c) Release of the mechanostimulated macrophages and C5A from the Hgel@C5A/MΦ in response to the ROS-enriched periodontitis microenvironment. (d) Mechanism of improving macrophage antimicrobial activity using Hgel@C5A/MΦ. (e) Illustration of reactivating *in-situ* macrophages to kill intracellular *Pg*. (f) Diagram of the final therapeutic effect of periodontitis.

believed to block C5aR, a pivotal target manipulated by *Pg* [15], thus ensuring the killing ability of both the *ex-situ* and *in-situ* macrophages. Furthermore, the elevated ROS level due to sustained periodontal inflammation would trigger the cleavage of the ROS-responsive borate ester bonds in the hydrogel to release the mechanostimulated *ex-situ* macrophages and the C5A. Meanwhile, this ROS-triggered reaction with the hydrogel would reduce the ROS level to suppress the periodontal inflammation leading to tissue damage. Hopefully, the hydrogel-mediated synergistic therapy could offer a new opportunity to eliminate the keystone pathogen *Pg* for a better treatment of the intractable periodontitis.

2. Materials and methods

2.1. Fabrication of PVA-TSPBA hydrogels

TSPBA (3 wt%, 6 wt% and 9 wt%) dissolved in ultrapure water was mixed with aqueous PVA solution (9 wt%) at room temperature to form three types of PVA-TSPBA hydrogels with different crosslinking degree, and these hydrogels were utilized in characterization experiments. For cell experiments, the PVA and TSPBA were dissolved in a serum-free medium. Cells and C5A were resuspended in the PVA solution, followed by the addition of TSPBA to form a hydrogel. As for *in vivo* treatments, dual syringes loaded with PVA and TSPBA solutions were used to achieve direct injections of the hydrogels into periodontal pockets.

2.2. In vitro phagocytosis assay

RAW264.7 cells (1×10^6) were seeded on 12-well plates or encapsulated in the PVA-TSPBA hydrogels with different stiffness (in a total volume of 200 μL per gel). The non-encapsulated cells cultured in a basal medium with or without 100 μM of H_2O_2 were named as + H_2O_2 or Control, respectively. All encapsulated cells were cultured in a basal medium with 100 μM of H_2O_2 until the cells were completely released from the gels. The released cells were stained with 5 μg mL^{-1} CellMask™ (Invitrogen, USA) for 15 min (37 °C, normoxic conditions) to visualize cell membrane, followed by 10 μg mL^{-1} Hoechst33342 (Biosharp, USA) for 20 min to stain cell nucleus. At the same time, *Pg* was stained with 10 μM carboxyfluorescein succinimidyl ester (CFSE; Sigma, USA) for 1 h (37 °C, anaerobic conditions). Then the cells were challenged with the CFSE-labeled *Pg* (37 °C, normoxic conditions) at a multiplicity of infection (MOI) of 10:1 (*Pg* to RAW264.7 cells ratio) according to the published studies [15,28]. The phagocytic process was monitored and recorded by a PE-Operetta CLS high-content analysis system (PerkinElmer, USA) and the proportion of cells containing *Pg* was quantified by a flow cytometer (CytoFLEX, Beckman Coulter).

2.3. In vitro immunofluorescence assay

After pretreatment with the varying stiffness hydrogels, the cells were fixed and permeabilized in 4% paraformaldehyde (PFA) with 0.2% Triton X-100 for 15 min. For immunofluorescence assay, the cells were incubated with primary antibodies *anti*-Piezo1 or *anti*-p-Rac1 for 12–16 h at 4 °C after being blocked with goat serum for 30 min. The following day, the cells were labeled with corresponding secondary antibodies as well as DAPI. Fluorescence images were taken with a confocal microscope (Olympus FV3000, Japan).

2.4. In vitro actin polymerization assay

Actin polymerization assay was performed to detect cytoskeleton changes in the cells treated with the different stiffness hydrogels, with or without subsequent *Pg* stimulation (MOI = 10:1, 4 h). The polymerized form of actin (F-actin) was specifically stained with 100 nM phalloidin (catalog no. PHDR1, Cytoskeleton, Inc., USA) for 30 min following fixation and permeabilization. Fluorescence intensity and distribution of F-actin were evaluated using flow cytometry and a confocal microscope, respectively.

2.5. In vitro NO detection

All the RAW264.7 cells encapsulated in the hydrogels or seeded on plates were cultured in the basal medium with 100 μM of H_2O_2 to mimic pathologically periodontal microenvironment and trigger the gel-encapsulated cells release. Exogenous complement C5 was added at 10 nM in all groups and C5A was added at 1 μM in corresponding treated groups according to the published study [28]. Then, the cells were challenged with *Pg* for 4 h (MOI = 10:1, 37 °C, normoxic conditions) and a hypersensitive cell-permeable NO fluorescent probe DAF-FM DA (5 μM, 30 min, 37 °C) was used to visualize the intracellular NO. Visual images were collected using the confocal microscope and quantifiable results were recorded by a flow cytometer (CytoFLEX, Beckman Coulter).

2.6. In vitro bacterial killing activity

Pg (1×10^7) was exposed to the RAW264.7 cells (1×10^6) which were received different pretreatments as mentioned in the section of *"In vitro NO detection"* (MOI = 10:1, 37 °C, normoxic conditions). After that, the cells were centrifuged at 300×*g* for 5 min and both the precipitates and supernatants were retained. Then, the cells were lysed to release internalized *Pg* [15], and the cell lysates were mixed with the corresponding supernatants which contained non-internalization *Pg*. Gradient dilutions of the mixtures were cultured on blood agar plates in a 37 °C anaerobic incubator to enumerate the remaining viable *Pg*. The *in vitro* colony forming units (CFU) index of *Pg* was calculated according to the formula: CFU of each group/CFU of the PBS group × 100.

2.7. In vitro osteoclastogenesis assays

The RAW264.7 cells were received different pretreatments as mentioned in the section of *"In vitro NO detection"* and then were challenged with *Pg* (MOI = 10:1, 37 °C, normoxic conditions). The co-incubated supernatants were collected and used as the macrophage-conditioned media for the following osteoclastogenesis and osteogenesis experiments. Mouse bone marrow-derived macrophages (mBMDMs) (1.5×10^6 cells per well) were cultured in the co-stimulation media consisting of an osteoclastic induction medium (20 ng mL^{-1} M-CSF and 40 ng mL^{-1} RANKL) and the macrophage-conditioned medium with different treatments (half and half). After 5 d of culture, osteoclast-associated proteins in mBMDMs were determined by Western bolt (WB) analysis. The detailed procedures for WB were described in our previous publication [29]. Besides, the cells were stained by tartrate-resistant acid phosphatase (TRAP) using a TRAP staining kit (Sigma-Aldrich, St. Louis, MO, USA) according to the manufacturer's protocol. More than 3 nucleuses cells were regarded as osteoclast cells. Digital images were obtained under brightfield microscopy using Axio Observer microscope (Carl Zeiss, Oberkochen, Germany). As for the resorption pit assay, cells were seeded on the Bone Assay Surface Multiwell Plates (Corning Life Sciences, USA) and were cultured in the above-mentioned culture condition. After 10 d of culture, bone slices were observed and imaged under brightfield microscopy using Axio Observer microscope (Carl Zeiss, Oberkochen, Germany) and the percentage of resorption areas of the bone slices was analyzed in Image J software (NIH, Bethesda, MD, USA).

2.8. In vitro osteogenesis assays

MC3T3-E1 cells (8×10^5 cells per well) were cultured in the co-stimulation media consisting of an osteogenic induction medium and the above-mentioned macrophage-conditioned media with different treatments at a ratio of 2:1. Alkaline phosphatase assay (ALP) was

performed as early osteogenic evaluation at day 7. In brief, the cells were incubated in 5-bromo-4-chloro-3-indolyl-phosphate/nitro blue tetrazolium (BCIP/NBT; Beyotime) for 30 min, following fixation in 4% PFA for 30 min at room temperature. ALP-positive cells were observed under an Axio Observer microscope (Carl Zeiss, Oberkochen, Germany). For the quantitative analysis of ALP, the cells were lysed in 1% Triton X-100 solution for 1 h, and the supernatant was taken after low-speed centrifugation (1500 rpm, 5min). The supernatant was detected by the Alkaline phosphatase kit (Jiancheng, China) according to the instructions. The absorbance was determined at 520 nm using a microplate reader (Biotek, Germany). Calcium accumulation, the late osteogenic marker, was assessed by Alizarin Red Staining after 21 d of above-mentioned co-stimulation. Cells were fixed in 4% PFA for 30 min, and then were stained with 40 mM Alizarin Red (pH 4.2; Cyagen, China) for another 30 min. After three washes with deionized water, ALP-positive cells were observed under the Zeiss Axio Observer microscope.

2.9. Animal model

All animal experiments were approved by the Ethics Committee of SUN-YAT-SEN University (SYSU-IACUC-2022-000239) and all procedures were followed the Laboratory Animal Protection Law. Four-week-old Sprague Dawley (SD) rats (male, 100–150 g) were randomly divided into five groups. Four groups of the rats were subgingival injected with a cocktail composed of LPS (1 mg mL^{-1}, 20 μL) and *Pg* (5×10^8 CFU mL^{-1}, 20 μL) at two-day intervals and five injections in total to establish periodontitis. Another group of healthy rats was maintained as the healthy control. Rat bone marrow-derived macrophages (rBMDMs) were prepared for the following cell therapy. Two days after the last LPS and *Pg* injection, the four groups of rats received 40 μL of saline, a C5A and rBMDMs mixture, a soft hydrogel loaded with C5A and rBMDMs and a stiff hydrogel loaded with C5A and rBMDMs, namely SHAM, C5A + MΦ, Lgel@C5A/MΦ and Hgel@C5A/MΦ, separately. The cell number was 1×10^6 per site and the amount of C5A was 5 μg according to the published study [30]. The therapeutic administration went once every 4 d for a total of 5 injections.

2.10. In vivo fluorescence imaging

Four days after the last therapy, the rats were anesthetized and depilated, followed by a subgingival injection of DCFH-DA (Beyotime, China) to evaluate the ROS levels in periodontal pockets [31]. A living small animal imaging system (Carestream *In Vivo* Imaging System FX PRO, USA) was used for fluorescence imaging of the rats, as well as quantification of the fluorescence intensity (510 nm excitation filter; 600 nm emission filter).

2.11. Micro-CT analysis

After fixation in 10% formalin for 48 h, all harvested maxillary tissues were scanned by a Micro-CT (SkyScan 1276, Bruker, Belgium). Three-dimensional reconstruction and two-dimensional imaging of the samples were used the SkyScan software CTvox and DataViewer, respectively. The linear evaluation on bone loss was used the average distances from cementoenamel junctions to the alveolar bone crest that is the lowest point of the palatal alveolar bone in experimental groups. And the volumetric changes on the alveolar bones were determined using the bone volume/total volume. The region of interest was confined in the palatal alveolar bone of the first maxillary molar and the quantitative analysis were performed using ImageJ software (version 1.53r, NIH, USA).

2.12. Statistics

Quantitative results were shown as means ± SD. All data were evaluated by one-way analysis of variance (ANOVA), followed by Tukey's multiple comparisons in Prism software (version 9.0, GraphPad, USA). $P < 0.05$ was taken as statistically significant.

3. Results

3.1. ROS levels in human saliva and gingival crevicular fluid (GCF)

It has been reported that ROS is overproduced in the progression of many inflammatory diseases [32], which is the major cause for oxidative stress-induced tissue damage. To assess the ROS levels in the periodontal microenvironment, the total oxidant status (TOS) of saliva and GCF in patients with periodontitis and healthy volunteers were measured by a TOS Colorimetric Assay Kit [33]. As shown in Fig. 2a, the TOS values of the periodontitis patients was elevated by 1.89-fold in saliva and 2.56-fold in GCF relative to those of the healthy volunteers. As the excessive ROS can accelerate periodontitis progression in multiple ways [34]. decreasing the local ROS level may be beneficial to periodontal healing. Moreover, the high ROS level in the periodontal microenvironment rationalized our design for a ROS-responsive hydrogel to control the payload release and consume the local ROS simultaneously.

3.2. Fabrication and characterization of ROS-responsive hydrogels

A ROS-responsive hydrogel was prepared *via* cross-linking PVA with N^1-(4-boronobenzyl)-N^3-(4-boronophenyl)-N^1,N^1,N^3,N^3-tetramethylpropane-1,3-diaminium (TSPBA). The ^{1}H NMR spectrum of TSPBA well matched its desirable chemical structure (Fig. S1), which confirmed the successful synthesis of the ROS-sensitive linker. As shown in Fig. 2b, three hydrogels were formed by mixing 9 wt% PVA with 3 wt%, 6 wt% and 9 wt% TSPBA, respectively. In the rheological tests (Fig. 2c), all of them showed higher storage moduli (G′) than loss moduli (G″), indicating the formation of a flexible hydrogel rather than a viscous liquid. Moreover, both the storage moduli (G′) and loss moduli (G″) increased considerably with increasing crosslinker (TSPBA) content from 3 to 9 wt %. The elastic modulus of hydrogels was measured on a universal testing machine. As shown in Fig. 2d, the compressive resistance stress of the hydrogels increased against their strain over the 0–40% range, in a TSPBA content-dependent manner. The elastic moduli of the three hydrogels were calculated from Fig. 2d, which showed that they were measured 1.74 ± 1.89 kPa, 27.08 ± 0.14 kPa and 106.53 ± 15.83 kPa as the elastic modulus corresponding to 3%, 6% and 9% TSPBA crosslinker, respectively (Fig. 2e). On the basis of their distinct compressive mechanical properties, the hydrogels containing 3%, 6% and 9% TSPBA were named as soft, medium and stiff hydrogels, respectively.

Next, the interior structure of the hydrogels was revealed by SEM observation as shown in Fig. 2f. Each hydrogel exhibited clear pore structure, and the pore size was decreased with increasing the crosslinker content due to the increased crosslinking density. Equilibrium water content (EWC) and swelling kinetics assays were performed to evaluate water absorption capacities of the hydrogels. All of them displayed the EWC values above 70% (Fig. 2g) and the swelling ratio above 290% (Fig. 2h), implying that these hydrogels had similarly high hydrophilicity. Since the microporous structure and highly hydrated state of the hydrogels are favorable for nutrient diffusion to support cell survival and growth, these hydrogels could be an ideal platform for cell delivery.

To confirm their ROS-responsive properties, the hydrogels were immersed in H_2O_2 solutions and their changes in weight and morphology were monitored. As shown in Fig. 2i, all the three groups of the hydrogels exhibited a fast weight loss in the presence of 1 mM of H_2O_2. When the H_2O_2 concentration was adjusted to 100 μM to mimic pathologically periodontal microenvironment, the hydrogels gradually turned smaller and transparent over time, finally disappearing at 120 h (Fig. S2). In contrast, negligible changes in shape and size were observed when the hydrogels were immersed in PBS. These results demonstrated that the hydrogels underwent a ROS-triggered degradation, which is

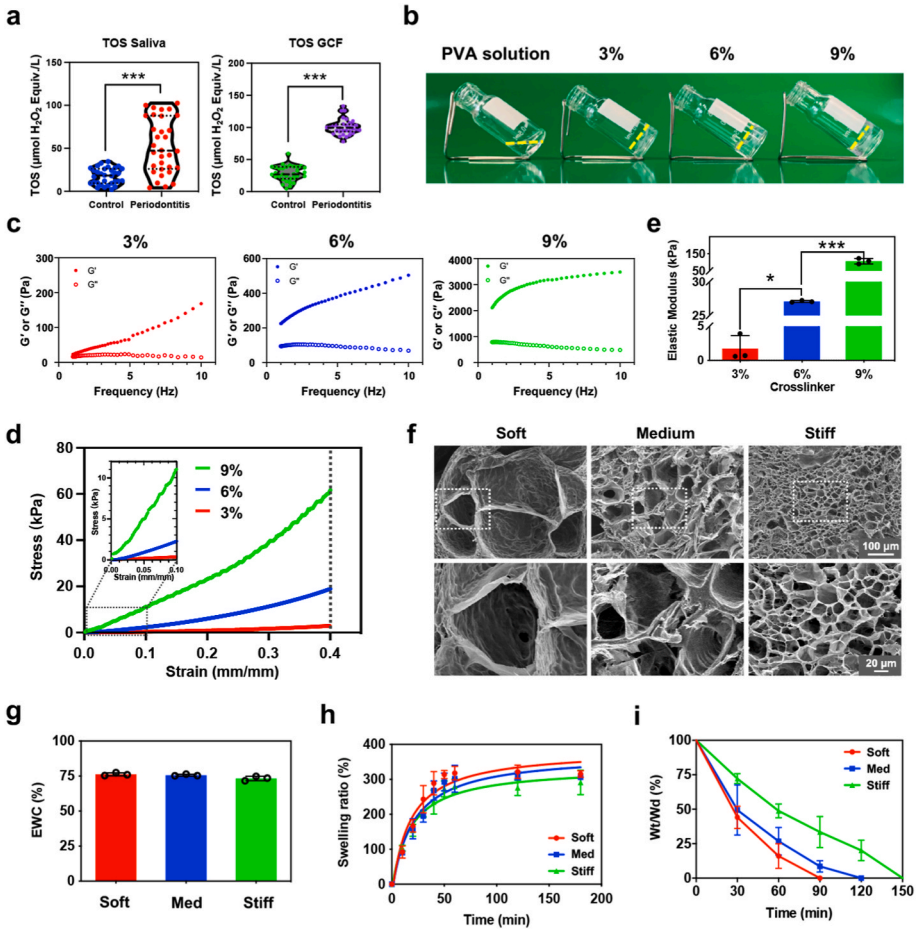

Fig. 2. Concentrations of total oxidative status (TOS) in clinical samples and characterization of ROS-sensitive hydrogels. (a) TOS measured in saliva (left panel) and gingival crevicular fluid (GCF) (right panel) in healthy subjects and periodontitis patients (n = 32, mean ± SD). (b) Photographs of PVA-TSPBA hydrogels with different crosslinking degrees. (c) Rheological frequency sweep of storage (G′) and loss (G″) moduli of the hydrogels. (d) Compression stress-strain curves of the hydrogels. (e) Elastic modulus of the hydrogels (n = 3, mean ± SD). (f) Representative SEM images of the hydrogels. (g) Equilibrium water content (EWC) of the hydrogels (n = 3, mean ± SD). (h) Swelling ratio of the hydrogels (n = 3, mean ± SD). (i) Degradation pattern of the ROS-sensitive hydrogels when immersing in 1 mM H_2O_2 solution (n = 3, mean ± SD). *$p < 0.05$; ***$p < 0.001$.

believed to assist an on-demand cell and drug release in the ROS-enriched periodontal microenvironment.

3.3. Hydrogels regulated phagocytic capability of macrophages

To verify the cytocompatibility of hydrogels, a live/dead assay was performed on RAW264.7 cells embedded in the hydrogels. Cells seeded on tissue culture plates were used as a control. As shown in Fig. 3a, most of the cells were stained green, and the cells being stained red were barely observed on day 5, indicating the good cytocompatibilities of these hydrogels. Further, a CCK-8 assay was also conducted to reconfirm their biosafety. As shown in Fig. S3, there was no significant difference in cell viability among all groups at each time point, which proved that co-incubating with the gels did not adversely affect the proliferation activity of RAW264.7 cells. Next, the cell-loaded hydrogels were transferred into the medium supplemented with 100 μM of H_2O_2 to investigate their cell release behaviors (Fig. 3b). The cell release rates were quantified by flow cytometry every 6 h until the complete disintegration of hydrogels was observed. The final numbers of cells released from each group were taken as their 100% separately. As shown in Fig. 3c, all the three hydrogels presented a time-dependent release pattern of RAW264.7 cells. Additionally, the stiff hydrogel showed a more sustained release pattern compared to the soft and medium ones. Due to sustained proliferation of cells inside the hydrogels, a higher total number of released cells was observed in the Stiff group compared with the two other groups at the end time points (Fig. S4). The released RAW264.7 cells from each group were separately collected, diluted to a consistent cell concentration, and finally used at 10^6 cells per well for the next treatments.

Engulfing pathogens is the first step in phagocyte-mediated host defense against bacterial invaders [17,35]. Since the phagocytic activity of macrophages has been proved susceptible to the stiffness of the matrix on which they were seeded [36,37], we further investigated whether the phagocytosis of the macrophages could also be affected when they were encapsulated inside the hydrogels with varying stiffness. To visualize the phagocytic process, the live RAW264.7 cells and *Pg* were pre-stained with the CellMask (red fluorescence) and CFSE (green fluorescence), respectively. Then, the RAW264.7 cells were challenged with the CFSE-labeled *Pg*, and the process was recorded by a time-lapse video microscopy. Encouragingly, the cells released from the stiff hydrogel, behaving like a strong "magnet" to capture bacteria, engulfed the majority of *Pg* near them. In sharp contrast, the cells cultured on regular plates ignored almost all the bacteria passing by them (Video S1 and Fig. 3d). Consistent results were obtained in flow cytometry analysis as well as in confocal microscopy images at a low-magnification view (Fig. 3e and Figs. S5a and b). That is, the stiffness of hydrogels contributed greatly to the phagocytic activity of macrophages, with the stiff hydrogel stimulation showing the highest proportion of *Pg*-positive cells (65.63% at 1h, 99.86% at 4h). In comparison, most of *Pg* escaped the phagocytosis of RAW264.7 cells in the H_2O_2-free and the H_2O_2-containing control groups, showing less than 20% *Pg*-positive cells after 4 h co-inoculation.

Supplementary data related to this article can be found at https://doi.org/10.1016/j.bioactmat.2023.01.011.

Piezo1 is a mechanically-gated ion channel that can sense a broad range of mechanical cues and consequently elicit divergent cellular outcomes [38]. Recent evidence suggests that activated Piezo1 can activate the Rho-family of GTPases member Rac1 [37], to modulate the rearrangements of actin cytoskeleton including polymerization of filamentous actin (F-actin) and lamellipodial protrusion, thereby triggering

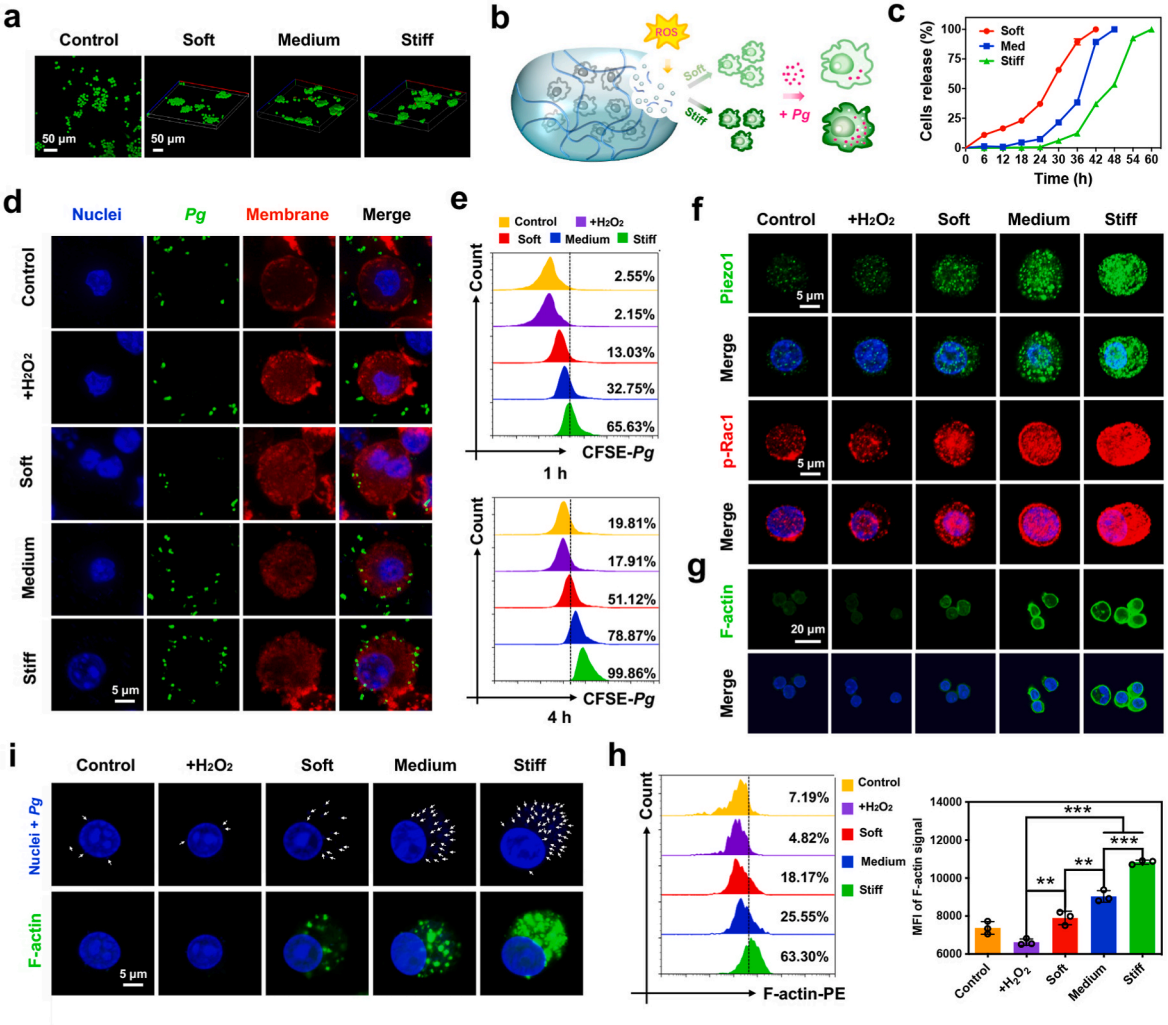

Fig. 3. Phagocytosis capability of macrophages encapsulated in hydrogels with different stiffness. (a) Calcein-AM/PI double staining of RAW264.7 cells cultured on tissue culture plates or encapsulated in hydrogels for 5 days. (b) Schematic illustration of the hydrogels with different stiffness regulating the phagocytosis capability of macrophages. (c) Release profiles of RAW264.7 cells from hydrogels at 100 μM of H_2O_2. (d) Confocal microscopy images showing phagocytosis of CFSE-labeled *Pg* by RAW264.7 cells. (e) Flow cytometry analyses of phagocytosis of CFSE-labeled *Pg* by RAW264.7 cells. (f) Confocal immunofluorescence images showing Piezo1 and p-Rac1 expressions in RAW264.7 cells. (g) Confocal immunofluorescence images showing F-actin expression in RAW264.7 cells. (h) Flow cytometry and quantitative analyses showing F-actin expression of RAW264.7 cells stained with phalloidin (n = 3, mean ± SD). (i) Confocal microscopy images of RAW264.7 cells stained with phalloidin (indicative of F-actin) after infection with *Pg* for 4 h. The white arrows indicate the internalized *Pg*. $^{**}p < 0.01$; $^{***}p < 0.001$.

the phagocytic action [39,40]. To explore whether the substrate stiffness affected phagocytosis of macrophages *via* this pathway, we measured the expression levels of Piezo1 and p-Rac1 in RAW264.7 cells seeded on the culture plates or encapsulated within the hydrogels using immunofluorescence staining and Western blot assays. Interestingly, Fig. 3f showed that the expression levels of Piezo1 in all the hydrogel-confined cells were higher than those in the cells seeded on the regular culture plates, probably owing to the omni-directional cell-matrix interactions rendered by the hydrogel-based three-dimensional matrices [41]. Moreover, the increase in Piezo1 expression was stiffness-dependent. The expression of Piezo1 was most effectively upregulated in the cells loaded inside the stiff hydrogel, which accordingly resulted in the highest expression level of the downstream protein p-Rac1. Semi-quantitative analysis of mean fluorescence intensity and Western blot assay also proved the stiffness-mediated positive effects on Piezo1 and p-Rac1 expressions (Figs. S6a and S6b). Finally, phalloidin staining was performed to label F-actin for assessing the actin polymerization under a confocal microscope. As shown in Fig. 3g, the expression of F-actin in RAW264.7 cells increased along with an increase in hydrogel stiffness. Quantitative analysis with flow cytometry was also highly supportive of the above results (Fig. 3h). Obviously, the elevated polymerized actin in the cells implied that the macrophages was mechanically activated for engulfing exogenous pathogens. Consequently, upon *Pg* stimulation (Fig. 3i), the cells from the stiff group exhibited heavy aggregation of F-actin around the bacterial adhesion sites, which accounted for the greatly facilitated bacterial internalization.

3.4. C5aR blockade enhanced the bactericidal ability of hydrogel-engineered macrophages

In consideration that C5aR blockade can counteract the *Pg*-induced debilitating effect on the killing activity of macrophages to boost the production of nitric oxide (NO) [15,42], we assessed the intracellular NO level of macrophages inside the hydrogel co-loaded with C5A, using a hypersensitive fluorescent probe for NO (DAF-FM DA). As shown in Fig. 4a, after 4 h *Pg* stimulation, the green fluorescence indicating NO-positive signals was hardly observed in RAW264.7 cells incubated in C5A-free culture medium (*i.e.*, the Free MΦ group), meaning the neglectable NO production in these cells under *Pg* invasion. On the contrary, the green fluorescence signal became visible when RAW264.7 cells

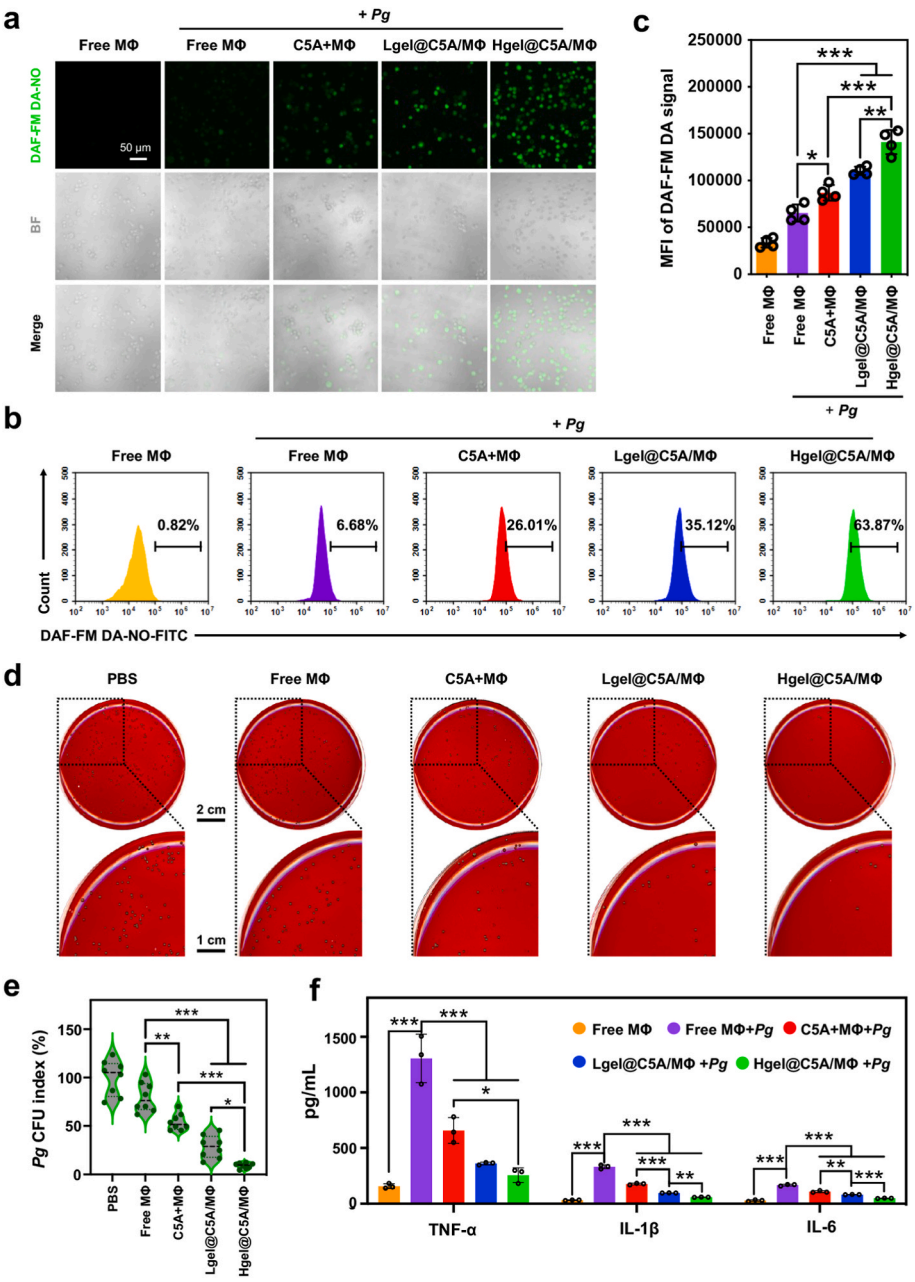

Fig. 4. Hgel@C5A/MΦ promoted *Pg* clearance and relieved *Pg*-induced inflammation *in vitro*. (a) Visualization of intracellular NO in RAW264.7 cells receiving different treatments on confocal microscope using DAF-FM DA as a probe. The MOI (*Pg* to RAW264.7 cells ratio) = 10:1. The C5A concentration: 1 μM. Flow cytometry (b) and quantitative analyses (c) of NO production by RAW264.7 cells receiving different treatments (n = 4, mean ± SD). (d) Photographs of the black bacterial colony on blood agar plates. (e) Quantitative analyses showing the colony forming units (CFU) of residual live bacteria (n = 8, mean ± SD). (f) Quantitative analyses of TNF-α, IL-1β and IL-6 expressions by ELISA kits in supernatants of culture media after RAW264.7 cells received different treatments (n = 3, mean ± SD). $^{*}p < 0.05$; $^{**}p < 0.01$; $^{***}p < 0.001$.

were treated with free C5A (the C5A + MΦ group), C5A-coencapsulated soft hydrogel (the Lgel@C5A/MΦ group) or C5A-coencapsulated stiff hydrogel (the Hgel@C5A/MΦ group). Similarly, flow cytometry assay (Fig. 4b) showed that only 6.68% of the cells were NO positive in the Free MΦ group after *Pg* infection, while the proportion of NO-positive cells increased to 26.01% when the cells were pretreated with C5A. Surprisingly, the Hgel@C5A/MΦ treatment further increased the positive proportion to 63.87%. The mean fluorescence intensity of NO quantified by flow cytometry showed a consistent trend (Fig. 4c). That is, pretreatment with the C5A-embeded hydrogels significantly increased the *Pg*-induced NO production in RAW264.7 cells, with the C5A-embeded stiff hydrogel (Hgel@C5A/MΦ) evidencing the highest efficacy. These results were reasonable as we have demonstrated mechanostimulation *via* adjusting hydrogel stiffness could promote the actin polymerization which is known as a key step for engulfing exogenous pathogens [40], and meanwhile C5A could effectively block the *Pg*-resulted inhibition on the bacterial killing capacity of RAW264.7 cells. Consequently, the most NO production was provoked in this event.

Next, the direct bactericidal effectiveness was evaluated after exposing *Pg* to RAW264.7 cells and then quantifying the viable bacteria by colony-forming unit (CFU) assay, using PBS-treated *Pg* as a control. Nearly 80% of *Pg* remained alive in the Free-MΦ group, whereas only 50% *Pg* survived when it was challenged with the MΦ pretreated with C5A (Fig. 4d and e). These results not only indicated the synergistic action of macrophages and C5A but also implied that the C5A released from the hydrogel would possess the potential to reactivate *in-situ* macrophages for *Pg* killing. More strikingly, the Hgel@C5A/MΦ group showed the lowest *Pg* survival rate less than 10%, which was highly supportive of our hydrogel-based therapeutic strategy.

In addition to enhancing bacterial clearance, C5A, as an antagonist of its complement receptor, could block inappropriate complement activation, thus reducing an overamplified inflammatory response [14]. Hence, three typical pro-inflammatory cytokines implicated in bone loss in periodontitis (TNF-α, IL-1β and IL-6) [43] were determined by enzyme-linked immunosorbent assay (ELISA). As shown in Fig. 4f, *Pg* stimulated RAW264.7 cells to secrete large amounts of TNF-α, IL-1β and

IL-6, while this pro-inflammatory response was significantly weakened upon C5aR blockade. Intriguingly, the production of these cytokines was further reduced in the presence of ROS-responsive hydrogels, implying that ROS removal may also contribute to the alleviation of ROS-induced inflammatory response. Collectively, the hydrogel-mediated modulation of macrophages in combination with C5aR blockade (C5A) presented much stronger anti-bacteria and anti-inflammation effects, which resulted in a decline of pro-inflammatory cytokines even further reducible through local ROS consumption by the ROS-sensitive hydrogel.

3.5. Macrophage-conditioned medium from the Hgel@C5A/MΦ treatment group maintained the bone homeostasis in vitro

Another intractable problem of periodontitis treatment is that bacteria-induced inflammation disrupts alveolar bone homeostasis, resulting in inflammation-driven bone loss [44]. Therefore, we further investigated if this combination strategy could help maintain the osteoclast-osteoblast balance against *Pg* infection given its effective anti-inflammation. Mouse bone marrow-derived macrophages (mBMDMs) were cultured in the macrophage-conditioned media from different treatments to explore the effects on osteoclastogenesis. Western blot assay (Fig. 5a) and its semi-quantitative results (Fig. S7) showed that among all *Pg* infection groups, mBMDMs of the Free MΦ group saw the highest expression levels of cathepsin K and MMP-9 (the osteoclast-specific marker proteins). In comparison, mBMDMs in other treated groups all showed less increases in cathepsin K (CTSK) and MMP-9 expressions to some extents. Excitingly, mBMDMs of the Hgel@C5A/MΦ group exhibited distinctly low expression levels of these two proteins like those of the control. TRAP staining and bone resorption pit (BRP) assay were also performed to assess the osteoclast formation and function in different conditioned media, respectively. The supernatant from the Free MΦ group with *Pg* infection induced giant multi-nucleated osteoclasts at 5 d of culture (Fig. 5b), and correspondingly huge resorption lacunas (43.87 ± 5.30 μm) were observed at 10 d (Fig. 5c). In contrast, osteoclastogenesis was strongly inhibited when mBMDMs were cultured in the supernatant from the Hgel@C5A/MΦ group with *Pg* infection, whose TRAP-positive osteoclasts and bone resorption areas (4.03 ± 0.81 μm) were dramatically decreased (Fig. 5b and c). These results suggested that the osteoclast differentiation and activation under the *Pg*-induced inflammation were effectively inhibited by our combination therapy.

In addition, osteoblast-derived factors receptor activator of NF-κB ligand (RANKL) and osteoprotegrin (OPG), as pivotal paracrine signaling biomolecules, also direct osteoclast behaviors. The balance between RANKL and OPG, which is highly sensitive to ROS and inflammatory cytokines [45], determines the fate of osteoclast precursors [46], and a high RANKL/OPG ratio promotes osteoclast differentiation and activation [47]. Therefore, we detected the levels of these two key cytokines in MC3T3-E1 cells (mouse osteoblasts) incubated for 7 d with a mixed culture medium consisting of an osteogenic medium and the above-mentioned supernatant (at a ratio of 2:1). According to the ELISA assays (Fig. 5d), the supernatant from the Free MΦ group with *Pg* infection induced MC3T3-E1 cells to secrete excessive RANKL but obviously inadequate OPG, as compared to the supernatant from the Free MΦ group without *Pg* infection. However, the RANKL expression was significantly suppressed when the MC3T3-E1 cells were cultured in the supernatants from other groups (*i.e.,* C5A + MΦ, Lgel@C5A/MΦ and Hgel@C5A/MΦ) with *Pg* infection. Furthermore, the OPG expression was increased up to the level of control when the MC3T3-E1 cells were cultured in the supernatant from the Hgel@C5A/MΦ group with *Pg* infection. The RANKL/OPG ratio of each group was also quantified in Fig. 5d to clarify the results. Briefly, the RANKL/OPG ratio showed a remarkable increase when the MC3T3-E1 cells was treated with the supernatant from the Free MΦ group with *Pg* infection, whereas the ratio could be significantly decreased when the Hgel@C5A/MΦ pretreatment

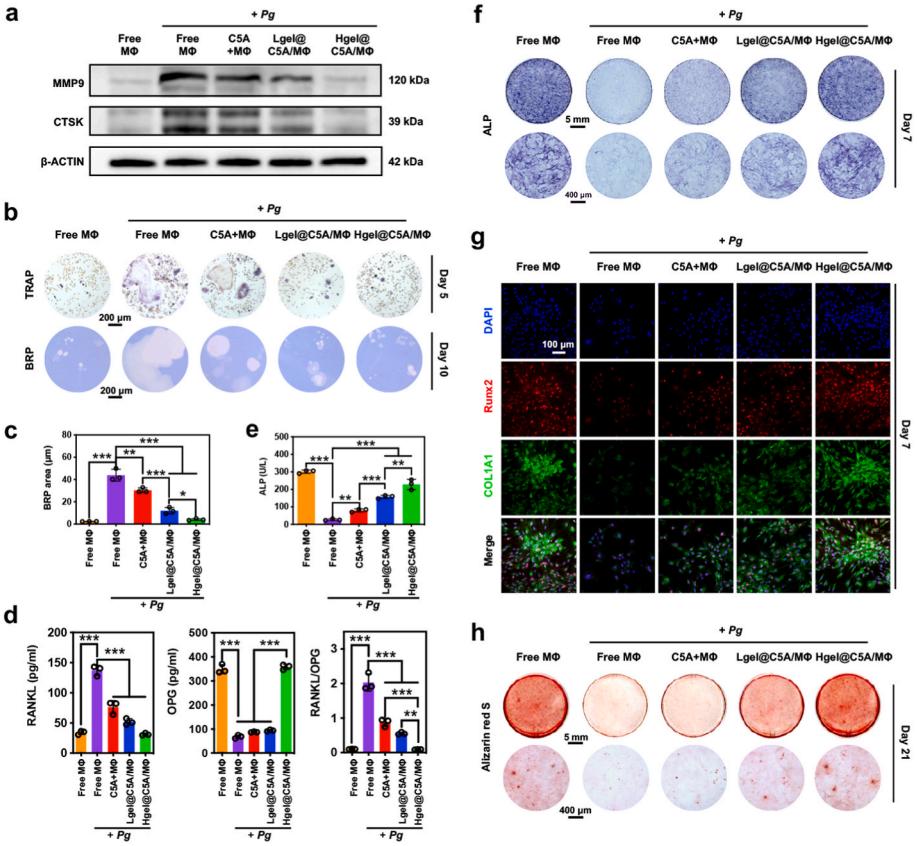

Fig. 5. Modulation of bone homeostasis using macrophage-conditioned culture media collected after RAW264.7 cells received different treatments *in vitro*. (a) Western blot assay of the MMP-9 and CTSK protein expressions in mBMDMs on day 5. (b) Representative TRAP staining images of mBMDMs on day 5 (upper panel) and bone resorption pits (BRP) images of mBMDMs on day 10 (lower panel). (c) Quantitative analysis of the BRP areas measured by ImageJ software (n = 3, mean ± SD). (d) Secretion of RANKL and OPG by MC3T3-E1 cells measured by ELISA kits on day 7, as well as the RANKL/OPG ratio. Quantitative analyses of ALP activity (e) and representative ALP staining images (f) of MC3T3-E1 cells on day 7 (n = 3, mean ± SD). (g) Representative confocal immunofluorescence images showing Runx2 (red) and COL1A1 (green) protein expressions in MC3T3-E1 cells on day 7. (h) Representative Alizarin red S staining images of MC3T3-E1 cells on day 21. $^{*}p < 0.05$; $^{**}p < 0.01$; $^{***}p < 0.001$.

was involved. These data supported that our combination therapy could also mediate the RANKL/OPG ratio to resist unfavorable osteoclast activation.

Then, we investigated the influences of the above macrophage-conditioned media on osteogenic differentiation of MC3T3-E1 cells. Early osteogenic activity was measured by alkaline phosphatase (ALP) staining and semiquantitative ALP assay at 7 d. As shown in Fig. 5e and f, the supernatant from the Free MΦ group with *Pg* infection obviously suppressed the ALP production in the MC3T3-E1 cells as compared to that from the Free MΦ group without *Pg* infection. However, the ALP activity exhibited 2.99-fold, 5.86-fold and 8.49-fold increases in cells incubated with the supernatants from the C5A + MΦ group, the Lgel@C5A/MΦ group and the Hgel@C5A/MΦ group, respectively, as compared with that of the cells incubated with the supernatant of the Free MΦ group with *Pg* infection. In addition, the expression levels of runt-related transcription factor 2 (Runx2) and collagen type I alpha 1 (COL1A1), specific early markers of osteogenic differentiation, were also detected by immunofluorescence staining and Western blot assays at 7 d of culture. As shown in Fig. 5g, the MC3T3-E1 cells showed the weakest red (Runx2) and green (COL1A1) fluorescence signals when they were cultured in the supernatant of the Free MΦ group with *Pg* infection, implying that *Pg*-induced inflammation would inhibit early osteoblast differentiation. In contrast, both the red and green fluorescence signals increased significantly in cells cultured in the supernatant from the Hgel@C5A/MΦ group with *Pg* infection, turning almost the same as the control group (*i.e.,* the Free MΦ group without *Pg* infection). Semi-quantitative analysis of mean fluorescence intensity and Western blot assay revealed consistent results (Figs. S8a and S8b). Alizarin Red S staining was performed to evaluate calcium deposit at 21 d (Fig. 5h). Compared to the cells incubated in the supernatant from the Free MΦ group with *Pg* infection, the cells incubated in the supernatant from the Hgel@C5A/MΦ group showed much larger and deeply stained mineralized nodules.

Taken together, the above *in vitro* results demonstrated that *Pg* infection not only promoted osteoclast formation, maturation and bone resorption but also suppressed osteoblastic differentiation. Encouragingly, our combination therapy strategy could counteract the adverse impacts on the osteoclast-osteoblast balance caused by *Pg* infection owing to the potent anti-inflammation properties of Hgel@C5A/MΦ.

3.6. Biosafety, degradation behavior and ROS scavenging capacity of hydrogels in vivo

Because of the excellent bactericidal and anti-inflammation performance of the combination strategy *in vitro*, we further investigated whether the combination therapy strategy would still work *in vivo*. Prior to using it in orthotopic periodontitis, the biocompatibility and biodegradability of the hydrogels were determined *in vivo*. First, PVA and TSPBA solution were injected subcutaneously into the backs of Sprague Dawley (SD) rats to form soft or stiff hydrogels. After 5 d, H&E staining images showed few inflammatory cells at the tissue-gel interface, indicating excellent biocompatibility of the hydrogels *in vivo* (Fig. 6a). Then, degradation behaviors of the ROS-responsive hydrogels *in vivo* were determined in rat subcutaneous inflammatory model. As shown in Fig. 6b, the soft and stiff hydrogels showed complete degradation at 3 d and 4 d post-injection, respectively. According to the degradation rate, the therapeutic administration was conducted once every 4 d for a total of 5 injections into the periodontal infectious sites (Fig. 6c and Fig. S9). In addition, rat bone marrow-derived macrophages (rBMDMs) were prepared from primary cultures of bone marrow extracted from tibiae and femurs of SD rats (see Supporting materials and methods for details). Immunocytochemistry identification presented that more than 96% of them was CD68 positive (Fig. S10), indicating the highly purified rBMDMs were successfully obtained. In the next experiments, SD rats were randomly divided into five groups to receive different treatments. Apart from the healthy control, the rest four groups were infected with *Pg* first and then received treatments of saline (Sham), C5A and rBMDMs (C5A + MΦ), the soft hydrogel loaded with C5A and rBMDMs

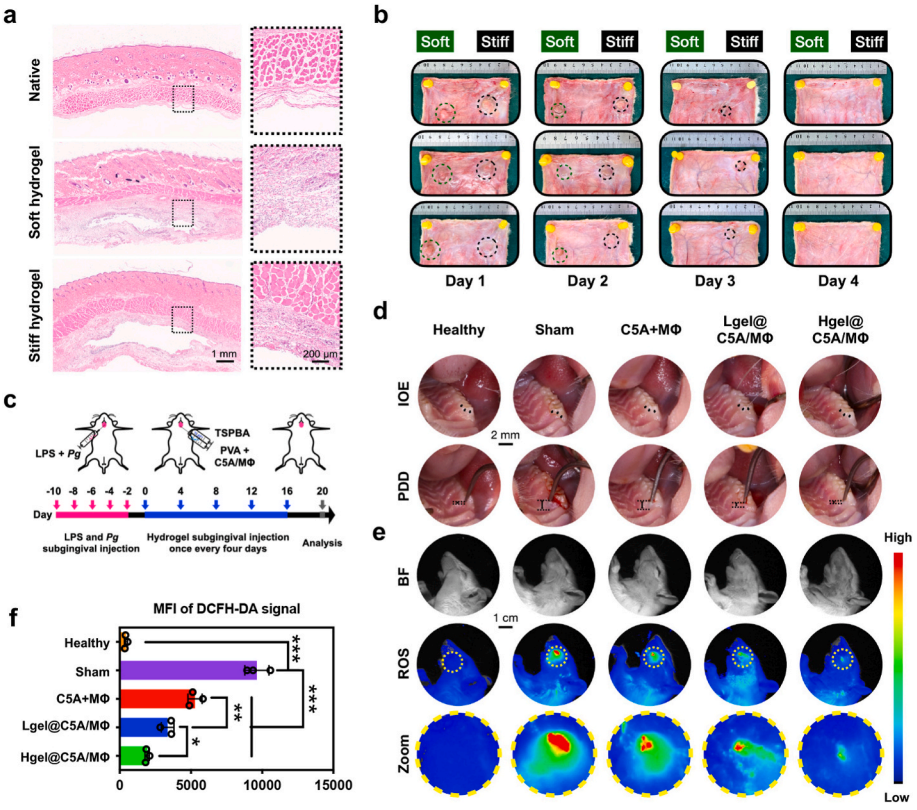

Fig. 6. *In vivo* biosafety, degradation behavior and ROS-scavenging capacity of stiffness-varied hydrogels. (a) Representative H&E staining images of subcutaneous hydrogels after being implanted for 5 days. (b) Photographs of *in vivo* degradation behavior of hydrogels. (c) Schematic illustration of constructing periodontitis SD rat model and *in vivo* therapeutic study. (d) Representative photographs of periodontal probing examinations at the infection site of SD rats receiving different treatments. IOE, intra-oral examination; PPD, probing pocket depth. The black arrows of IOE images indicated the gingival margin position. The black dashed lines and arrows in PPD images indicate the probing depth. Cell number, 1×10^6 rBMDMs per site. The injection amount of C5A was 5 μg per site. (e) *In vivo* fluorescence imaging showing ROS levels at the infected site of SD rats after different treatments. (f) Quantitative analyses of ROS levels based on mean fluorescence intensity of DCFH-DA (n = 3, mean ± SD). $^*p < 0.05$; $^{**}p < 0.01$; $^{***}p < 0.001$.

(Lgel@C5A/MΦ) and the stiff hydrogel loaded with C5A and rBMDMs (Hgel@C5A/MΦ), respectively.

After the last treatments ended for 4 d, intra-oral examination (IOE), probing pocket depth (PPD) and bleeding on probing (BOP) were performed to evaluate the degrees of inflammation in periodontal tissues of the rats. As shown in Fig. 6d, rats treated with saline (the Sham group) showed obviously swollen gums (black arrows) as well as the strongest positive reactions for BOP and deepest periodontal pockets (black arrows) among all groups. Other therapeutic groups, especially the Hgel@C5A/MΦ group, presented relatively healthy gums with slight periodontal pocket formation and minor bleedings. In addition, DCFH-DA, a fluorescent probe for ROS, was injected *in situ* and the fluorescence signal was recorded by an *in vivo* fluorescence imaging system to indicate the ROS accumulation in periodontal tissues. As shown in Fig. 6e and f, rats receiving saline (the Sham group) exhibited a strong fluorescence signal in the periodontal infected sites, indicating an enriched ROS in their periodontal tissues. However, delivering C5A + MΦ to periodontal sites could attenuate the fluorescence signal, indicating a reduced inflammation. Moreover, compared to the Sham group, the Hgel@C5A/MΦ-treated group showed a significantly decreased fluorescence intensity by 80% due to the excellent antimicrobial activity and great ROS scavenging capacity.

3.7. Therapeutic effects of Hgel@C5A/MΦ on periodontitis in vivo

To further evaluate the efficacy of Hgel@C5A/MΦ in treating periodontitis *in vivo*, the rats were sacrificed at 4 d after ending the treatment and the unilateral maxillary tissue was harvested for micro-CT analysis. As shown in Fig. 7a, *Pg* infection resulted in severe bone loss in the saline-treated SD rats (the Sham group), in sharp contrast with the Hgel@C5A/MΦ-treated rats that were resistant to *Pg*-induced bone resorption. Linear measurement of the average CEJ-ABC distance quantitatively showed the level of periodontal bone loss in each group (Fig. 7b). The Sham group exhibited above one-fold increase in the CEJ-ABC distance relative to the healthy control (1550.0 ± 125.30 μm *vs* 700.0 ± 52.9 μm), whereas all therapeutic groups significantly reduced the *Pg*-induced bone loss. The shortest CEJ-ABC distance was observed in the Hgel@C5A/MΦ group (950.0 ± 45.83 μm). Besides, the Hgel@C5A/MΦ group also exhibited significantly higher bone quality than that of the other treatment groups in the quantitative BV/TV results (Fig. 7c).

H&E and immunohistochemical staining of the infected molars further supported the osteoprotective effects of the Hgel@C5A/MΦ group. As shown in Fig. 7d, the rats receiving saline (the Sham group) developed apparent bone defects, showing a typical moth-eaten appearance at the palatal sides of alveolar bone (Fig. 7d, upper panel) and a great number of TNF-α, IL-1β and IL-6 positive cells around the erosion sites (Fig. 7d, lower panel). However, the expressions of these proinflammatory effectors were considerably diminished in the rats receiving Hgel@C5A/MΦ, which was consistent with the protective effect of the Hgel@C5A/MΦ therapy against *Pg*-induced bone loss. The semi-quantitative results clearly showed the discrepancy of the proinflammatory factor expressions in each group (Fig. S11). Since sustained inflammation could turn the osteoblast-osteoclast balance towards osteoclast-dominated bone resorption [46], immunofluorescent staining assay and its semi-quantitative analysis were performed to evaluate the

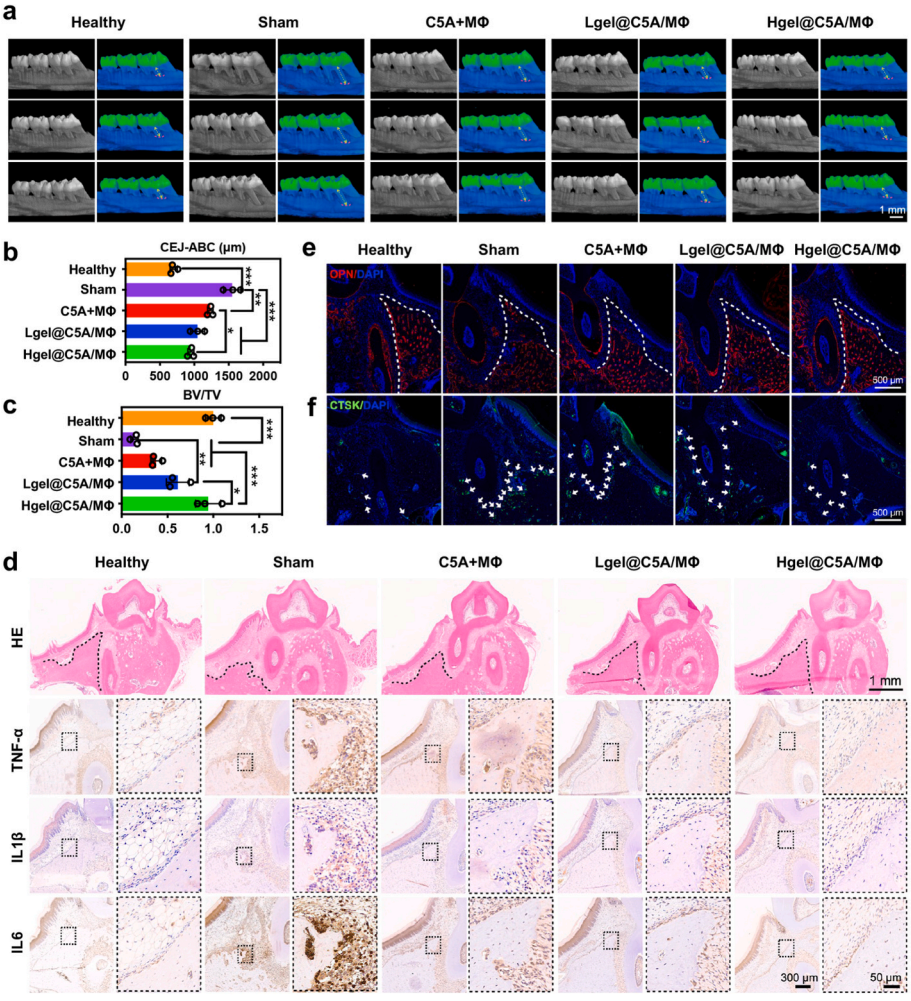

Fig. 7. *In vivo* evaluation of therapeutic efficacies after different treatments. (a) Three-dimensionally reconstructed Micro-CT images of the infected maxillary molar regions. The tooth crowns (enamel) were drawn in green, and the tooth roots (cementum) and alveolar bones were drawn in blue. The pink dashed lines indicate each alveolar bone crest. The yellow dotted arrows show the loss of periodontal bone height. Cell number, 1×10^6 rBMDMs per injection site. The amount of C5A was 5 μg per injection site. (b) The averaged distances from the cementoenamel junctions to the alveolar bone crest (CEJ-ABC) (n = 3, mean ± SD). (c) The ratio of bone volume to total volume (BV/TV) (n = 3, mean ± SD). (d) Upper panels show representative H&E staining images of coronal cross-sections of the infected first maxillary molars of SD rats. The black dashed lines indicate the margin of alveolar bone crest; lower panels show immunohistochemical staining of TNF-α, IL-1β and IL-6 in corresponding infected sites. (e) Immunofluorescence staining of OPN (red). The white dashed lines indicate the theoretically original alveolar bone height of each group referring to the healthy control. (f) Immunofluorescence staining of CTSK (green) protein expression. The white arrows show the CTSK-positive cells. *$p < 0.05$; **$p < 0.01$; ***$p < 0.001$.

expression levels of OPN and CTSK as the osteoblast- and osteoclast-specific markers, respectively, in the alveolar bone regions (Fig. 7e, f and Fig. S12). Specifically, the Sham group showed the least OPN-positive staining (red fluorescence) but the most CTSK-positive staining (green fluorescence). By comparison, the Hgel@C5A/MΦ group showed largely increased area of OPN-positive staining but considerably decreased area of CTSK-positive staining, like the healthy group. Consistent trends were observed in semi-quantitative analysis of immunofluorescence staining for OPN and CTSK as shown in Fig. S12. And the semi-quantitative agreement of these trends again confirmed that our combined therapy could help maintain the osteoclast-osteoblast balance against *Pg* infection.

Finally, the *in vivo* bactericidal effect was evaluated according to the *Pg* CFU index. As shown in Fig. S14, the rats receiving saline (the Sham group) showed the highest level of *Pg* colonization in their periodontal tissue. In comparison, the amount of *Pg* CFU was significantly decreased upon other treatments. Especially, the Hgel@C5A/MΦ group demonstrated the most prominent bactericidal effect according to its much lower *Pg* CFU amount than other treatment groups. Notably, the total *Pg* CFU level of this treatment group dropped down to that of the healthy group, indicating that, most likely, even those *Pg* hidden intracellularly were eradicated. These data implied that our combination therapy using Hgel@C5A/MΦ could effectively combat the *Pg*-driven periodontitis. Although both the C5A + MΦ treatment and the Lgel@C5A/MΦ treatment decreased the alveolar bone loss to some extents, they failed to completely prevent *Pg* colonization, meaning that a risk of infection recrudescence still exists.

4. Discussion

Periodontitis is admittedly a microbe-driven intractable infectious disease. As the most common adjuvant therapy for periodontitis, direct antimicrobial therapy encounters great problems since the currently available antimicrobials are hard to eradicate *Pg* hiding inside the deactivated immune cells [48,49]. Even worse, the residual periodontal bacteria may constantly elicit inflammatory responses to cause chronic damages of periodontal tissues, which results in loss of alveolar bone. In turn, the chronic inflammation may lead to a nutritionally conducive environment for the outgrowth of the periodontal pathogens, eventually causing a microflora disturbance and a periodontitis recurrence [50]. In comparison with the conventional antibiotic therapy, a new strategy which significantly strengthened the phagocytic and bactericidal activities of immune cells has great advantages to bypass the antibiotic resistance.

Macrophages, as one of the most important immune cells in the periodontal niche, are involved in pathogen clearance and homeostasis maintenance [51]. Unfortunately, *Pg* has evolved several mechanisms to subvert the macrophage functions, which selectively impaired the antimicrobial responses including phagocytosis and killing activity of macrophages without interfering their proinflammatory activity [2,15]. In the present study, the inability of *in-situ* macrophages in controlling *Pg* infection drove us to develop a synergistic therapeutic strategy which employed ROS-sensitive hydrogels to strengthen the antibacterial activity of macrophages for effective periodontitis treatment. First, we found that the stiffness of hydrogel affected the phagocytic activity of the embedded macrophages, based on which we achieved a desirable phagocytic activity at the elastic modulus of 106 kPa. At molecular level, we found that the stiff substrate upregulated the expression of Piezo1, known as a mechanotransducer [52], to convert the extracellular mechanical cues into the intracellular biochemical signals including Rac1 activation and cytoskeleton remodeling. Cytoskeleton remodeling is a hallmark of the phagocytic actions. In other words, the phagocytic receptor-ligand recognition and followed cascade signaling will trigger the F-actin polymerization and filopodia/podosome formation in the site of ingestion, thus allowing the internalization of bacteria [40]. According to our *in vitro* results, macrophages released from the stiff hydrogel possessed much higher F-actin polymerization at the bacterial adhesion sites than others, which accounted for the largest number of their ingested bacteria. Previous studies have shown that macrophages seeded on stiffer substrates had higher phagocytic activity [37,53], which are supportive of our results obtained in the three-dimensional cell culture model.

Then, C5A was incorporated into the macrophage-embedded hydrogel to unleash the antibacterial activity of macrophages through blocking the undesirable C5aR activation after *Pg* infection. Through the synergistic therapeutic design, the *ex-situ* macrophages released from the stiff hydrogel not only effectively engulfed *Pg* but also prevented the *Pg*-inducible C5aR activation so as to maintain a strong killing function over a long-term therapy. In addition, C5A released from the stiff hydrogel would also endow the *in-situ* deactivated macrophages with killing function again to eradicate those *Pg* hidden intracellularly [54], as implied by the *in vitro* experiment evidencing the better *Pg*-killing of macrophages assisted by C5A, as well as *in vivo* experiment detecting the healthy group-equivalent *Pg* number in the synergistic treatment. Consequently, a potent bactericidal effect is achievable. Finally, through the ROS-responsive design of the hydrogel, the accumulated ROS in the periodontal niche could be directly removed, which further mitigated the periodontal inflammation to augment the protection against the periodontal bone loss.

Cell therapy has seen an explosive growth in both basic research and clinical practice over the last few decades [55,56]; yet using this approach to reverse severe periodontitis is still in its infancy. In this work, we successfully applied a synergistic macrophage-based therapy (*i.e.,* rBMDMs in combination with a stiffness-tuned hydrogel and a commercially available C5A) to a rat model of periodontitis, and this therapy exhibited apparently superior therapeutic efficiency to others, including the lowest bacterial load, the mildest periodontal inflammation and the strongest bone protective effect. In addition to the prominent therapeutic effects, the cost-effective raw materials and the facile fabrication approach also render this synergistic cell therapy a great potentiality for clinical translation in the future. When this strategy is used clinically, with consideration of a relatively high yield of macrophages in bone marrow [57], the macrophages can be obtained from the patients' own bone marrow, purified *in vitro,* and infused back into the same patient. Using this autologous cell source can not only reduce ethical issues, but also circumvent immune rejection so as to ensure the safety of this strategy. Additionally, unlike other cell-based therapies such as chimeric antigen receptor (CAR)-T or T-cell receptor (TCR)-T cell therapy, this work does not involve any gene alterations or cellular reprogramming both *in vitro* and *in vivo* [58,59], further bypassing the inevitable ethical problems surrounding gene-edited transplantation cells.

In summary, we proposed a stiffness-tuned and ROS-responsive hydrogel for codelivery of macrophages and C5A to treat periodontitis. Our work highlights the importance of using mechanical cues to manipulate cell fates, which is an emerging and promising way redirecting donor cells to combat intractable diseases or to achieve tissue regeneration.

Ethics approval statement

All animal experiments were approved by the Ethics Committee of SUN-YAT-SEN University (SYSU-IACUC-2022-000239) and all procedures were followed the Laboratory Animal Protection Law.

Patient consent statement

All the patients and the healthy volunteers gave written informed consent, and the protocols were approved by the Medical Ethics Committee of Hospital of Stomatology SUN-YAT-SEN University (KQEC-2022-05-01).

Data availability

Correspondence and requests for materials should be addressed to corresponding author. All data needed to evaluate the conclusions in the paper are present in the paper and the Supporting Information. Additional data related to this paper may be requested from the authors.

CRediT authorship contribution statement

Ziqi Gan: Investigation, Methodology, Software, Data curation, Formal analysis, Writing – original draft. **Zecong Xiao:** Investigation, Data curation, Project administration, Supervision, Writing – review & editing. **Zhen Zhang:** Investigation, Methodology, Software, Writing – review & editing. **Yang Li:** Investigation, Methodology. **Chao Liu:** Investigation, Methodology. **Xin Chen:** Methodology. **Yuanbo Liu:** Methodology. **Dongle Wu:** Methodology. **Chufeng Liu:** Supervision, Writing – review & editing. **Xintao Shuai:** Project administration, Supervision, Writing – review & editing, Funding acquisition. **Yang Cao:** Project administration, Resources, Supervision, Writing – review & editing, Funding acquisition.

Declaration of competing interest

The authors declare that they have no competing interests.

Acknowledgements

This work was supported by the National Natural Science Foundation of China (82170987, 81970963, 51933011, 31971296), the Natural Science Foundation of Guangdong Province (2021A1515012535) and the General Scientific Research Cultivation Project of Guanghua School of Stomatology, Sun Yat-Sen University (174-2018-XMZC-0001-03-0125/D-16).

Appendix A. Supplementary data

Supplementary data to this article can be found online at https://doi.org/10.1016/j.bioactmat.2023.01.011.

References

[1] N.J. Kassebaum, E. Bernabé, M. Dahiya, B. Bhandari, C.J. Murray, W. Marcenes, Global burden of severe periodontitis in 1990-2010: a systematic review and meta-regression, J. Dent. Res. 93 (11) (2014) 1045–1053.
[2] G. Hajishengallis, R.J. Lamont, Breaking bad: manipulation of the host response byPorphyromonas gingivalis, Eur. J. Immunol. 44 (2) (2014) 328–338.
[3] G. Hajishengallis, S. Liang, M.A. Payne, A. Hashim, R. Jotwani, M.A. Eskan, M. L. McIntosh, A. Alsam, K.L. Kirkwood, J.D. Lambris, R.P. Darveau, M.A. Curtis, Low-abundance biofilm species orchestrates inflammatory periodontal disease through the commensal microbiota and complement, Cell Host Microbe 10 (5) (2011) 497–506.
[4] R.J. Lamont, H. Koo, G. Hajishengallis, The oral microbiota: dynamic communities and host interactions, Nat. Rev. Microbiol. 16 (12) (2018) 745–759.
[5] G. Hajishengallis, The inflammophilic character of the periodontitis-associated microbiota, Mol. Oral. Microbiol. 29 (6) (2014) 248–257.
[6] P.I. Diaz, A. Hoare, B.Y. Hong, Subgingival microbiome shifts and community dynamics in periodontal diseases, J. Calif. Dent. Assoc. 44 (7) (2016) 421–435.
[7] N.B. Parahitiyawa, L.J. Jin, W.K. Leung, W.C. Yam, L.P. Samaranayake, Microbiology of odontogenic bacteremia: beyond endocarditis, Clin. Microbiol. Rev. 22 (1) (2009) 46–64.
[8] S.S. Dominy, C. Lynch, F. Ermini, M. Benedyk, A. Marczyk, A. Konradi, M. Nguyen, U. Haditsch, D. Raha, C. Griffin, L.J. Holsinger, S. Arastu-Kapur, S. Kaba, A. Lee, M. I. Ryder, B. Potempa, P. Mydel, A. Hellvard, K. Adamowicz, H. Hasturk, G. D. Walker, E.C. Reynolds, R.L.M. Faull, M.A. Curtis, M. Dragunow, J. Potempa, Porphyromonas gingivalis in Alzheimer's disease brains: evidence for disease causation and treatment with small-molecule inhibitors, Sci. Adv. 5 (1) (2019) eaau3333.
[9] G. Hajishengallis, T. Chavakis, Local and systemic mechanisms linking periodontal disease and inflammatory comorbidities, Nat. Rev. Immunol. 21 (7) (2021) 426–440.
[10] M. Wang, M.A. Shakhatreh, D. James, S. Liang, S. Nishiyama, F. Yoshimura, D. R. Demuth, G. Hajishengallis, Fimbrial proteins of porphyromonas gingivalis mediate in vivo virulence and exploit TLR2 and complement receptor 3 to persist in macrophages, J. Immunol. 179 (4) (2007) 2349–2358.
[11] M. Wang, G. Hajishengallis, Lipid raft-dependent uptake, signalling and intracellular fate of Porphyromonas gingivalis in mouse macrophages, Cell Microbiol. 10 (10) (2008) 2029–2042.
[12] A. Wilensky, R. Tzach-Nahman, J. Potempa, L. Shapira, G. Nussbaum, Porphyromonas gingivalis gingipains selectively reduce CD14 expression, leading to macrophage hyporesponsiveness to bacterial infection, J. Innate. Immun. 7 (2) (2015) 127–135.
[13] K. Elward, P. Gasque, Eat me" and "don't eat me" signals govern the innate immune response and tissue repair in the CNS: emphasis on the critical role of the complement system, Mol. Immunol. 40 (2) (2003) 85–94.
[14] S. Liang, J.L. Krauss, H. Domon, M.L. McIntosh, K.B. Hosur, H. Qu, F. Li, A. Tzekou, J.D. Lambris, G. Hajishengallis, The C5a receptor impairs IL-12-dependent clearance of Porphyromonas gingivalis and is required for induction of periodontal bone loss, J. Immunol. 186 (2) (2011) 869–877.
[15] M. Wang, J.L. Krauss, H. Domon, K.B. Hosur, S. Liang, P. Magotti, M. Triantafilou, K. Triantafilou, J.D. Lambris, G. Hajishengallis, Microbial hijacking of complement-toll-like receptor crosstalk, Sci. Signal. 3 (109) (2010) ra11.
[16] H. Hawlisch, Y. Belkaid, R. Baelder, D. Hildeman, C. Gerard, J. Köhl, C5a negatively regulates toll-like receptor 4-induced immune responses, Immunity 22 (4) (2005) 415–426.
[17] G. Weiss, U.E. Schaible, Macrophage defense mechanisms against intracellular bacteria, Immunol. Rev. 264 (1) (2015) 182–203.
[18] C.J. Bashor, I.B. Hilton, H. Bandukwala, D.M. Smith, O. Veiseh, Engineering the next generation of cell-based therapeutics, Nat. Rev. Drug Discov. 21 (9) (2022) 655–675.
[19] M. Guvendiren, J.A. Burdick, Engineering synthetic hydrogel microenvironments to instruct stem cells, Curr. Opin. Biotechnol. 24 (5) (2013) 841–846.
[20] S. Fuchs, A.U. Ernst, L.H. Wang, K. Shariati, X. Wang, Q. Liu, M. Ma, Hydrogels in emerging technologies for type 1 diabetes, Chem. Rev. 121 (18) (2021) 11458–11526.
[21] N. Oliva, J. Conde, K. Wang, N. Artzi, Designing hydrogels for on-demand therapy, Acc. Chem. Res. 50 (4) (2017) 669–679.
[22] Q. Shi, H. Liu, D. Tang, Y. Li, X. Li, F. Xu, Bioactuators based on stimulus-responsive hydrogels and their emerging biomedical applications, NPG Asia Mater. 11 (1) (2019) 64.
[23] F. Guilak, D.M. Cohen, B.T. Estes, J.M. Gimble, W. Liedtke, C.S. Chen, Control of stem cell fate by physical interactions with the extracellular matrix, Cell Stem Cell 5 (1) (2009) 17–26.
[24] N. Huebsch, E. Lippens, K. Lee, M. Mehta, S.T. Koshy, M.C. Darnell, R.M. Desai, C. M. Madl, M. Xu, X. Zhao, O. Chaudhuri, C. Verbeke, W.S. Kim, K. Alim, A. Mammoto, D.E. Ingber, G.N. Duda, D.J. Mooney, Matrix elasticity of void-forming hydrogels controls transplanted-stem-cell-mediated bone formation, Nat. Mater. 14 (12) (2015) 1269–1277.
[25] F. Guilak, D.L. Butler, S.A. Goldstein, F.P. Baaijens, Biomechanics and mechanobiology in functional tissue engineering, J. Biomech. 47 (9) (2014) 1933–1940.
[26] V. Kanoldt, C. Kluger, C. Barz, A.L. Schweizer, D. Ramanujam, L. Windgasse, S. Engelhardt, A. Chrostek-Grashoff, C. Grashoff, Metavinculin modulates force transduction in cell adhesion sites, Nat. Commun. 11 (1) (2020) 6403.
[27] A. Torres-Gomez, C. Cabañas, E.M. Lafuente, Phagocytic integrins: activation and signaling, Front. Immunol. 11 (2020) 738.
[28] T. Maekawa, J.L. Krauss, T. Abe, R. Jotwani, M. Triantafilou, K. Triantafilou, A. Hashim, S. Hoch, M.A. Curtis, G. Nussbaum, J.D. Lambris, G. Hajishengallis, Porphyromonas gingivalis manipulates complement and TLR signaling to uncouple bacterial clearance from inflammation and promote dysbiosis, Cell Host Microbe 15 (6) (2014) 768–778.
[29] Z. Gan, Y. Zhao, Y. Wu, W. Yang, Z. Zhao, L. Zhao, Three-dimensional, biomimetic electrospun scaffolds reinforced with carbon nanotubes for temporomandibular joint disc regeneration, Acta Biomater. 147 (2022) 221–234.
[30] T. Abe, K.B. Hosur, E. Hajishengallis, E.S. Reis, D. Ricklin, J.D. Lambris, G. Hajishengallis, Local complement-targeted intervention in periodontitis: proof-of-concept using a C5a receptor (CD88) antagonist, J. Immunol. 189 (11) (2012) 5442–5448.
[31] X. Bao, J. Zhao, J. Sun, M. Hu, X. Yang, Polydopamine nanoparticles as efficient scavengers for reactive oxygen species in periodontal disease, ACS Nano 12 (9) (2018) 8882–8892.
[32] V. De Caro, D. Murgia, F. Seidita, E. Bologna, G. Alotta, M. Zingales, G. Campisi, Enhanced in situ availability of aphanizomenon flos-aquae constituents entrapped in buccal films for the treatment of oxidative stress-related oral diseases: biomechanical characterization and in vitro/ex vivo evaluation, Pharmaceutics 11 (1) (2019) 35.
[33] J. Toczewska, M. Maciejczyk, T. Konopka, A. Zalewska, Total oxidant and antioxidant capacity of gingival crevicular fluid and saliva in patients with periodontitis: review and clinical study, Antioxidants 9 (5) (2020) 450.
[34] L.-J. Su, J.-H. Zhang, H. Gomez, R. Murugan, X. Hong, D. Xu, F. Jiang, Z.-Y. Peng, Reactive oxygen species-induced lipid peroxidation in apoptosis, autophagy, and ferroptosis, Oxid. Med. Cell. Longev. (2019), 5080843, 2019.
[35] Q. Jiang, Y. Zhao, Y. Shui, X. Zhou, L. Cheng, B. Ren, Z. Chen, M. Li, Interactions between neutrophils and periodontal pathogens in late-onset periodontitis, Front. Cell. Infect. Microbiol. 11 (2021), 627328.
[36] R. Sridharan, B. Cavanagh, A.R. Cameron, D.J. Kelly, F.J. O'Brien, Material stiffness influences the polarization state, function and migration mode of macrophages, Acta Biomater. 89 (2019) 47–59.

[37] J. Geng, Y. Shi, J. Zhang, B. Yang, P. Wang, W. Yuan, H. Zhao, J. Li, F. Qin, L. Hong, C. Xie, X. Deng, Y. Sun, C. Wu, L. Chen, D. Zhou, TLR4 signalling via Piezo1 engages and enhances the macrophage mediated host response during bacterial infection, Nat. Commun. 12 (1) (2021) 3519.
[38] J.L. Nourse, M.M. Pathak, How cells channel their stress: interplay between Piezo1 and the cytoskeleton, Semin. Cell Dev. Biol. 71 (2017) 3–12.
[39] D. Spiering, L. Hodgson, Dynamics of the Rho-family small GTPases in actin regulation and motility, Cell Adhes. Migrat. 5 (2) (2011) 170–180.
[40] S.A. Freeman, S. Grinstein, Phagocytosis: receptors, signal integration, and the cytoskeleton, Immunol. Rev. 262 (1) (2014) 193–215.
[41] B.M. Baker, C.S. Chen, Deconstructing the third dimension: how 3D culture microenvironments alter cellular cues, J. Cell Sci. 125 (Pt 13) (2012) 3015–3024.
[42] G. Hajishengallis, M. Wang, S. Liang, M. Triantafilou, K. Triantafilou, Pathogen induction of CXCR4/TLR2 cross-talk impairs host defense function, Proc. Natl. Acad. Sci. U. S. A. 105 (36) (2008) 13532–13537.
[43] X.Y. Zheng, C.Y. Mao, H. Qiao, X. Zhang, L. Yu, T.Y. Wang, E.Y. Lu, Plumbagin suppresses chronic periodontitis in rats via down-regulation of TNF-α, IL-1β and IL-6 expression, Acta Pharmacol. Sin. 38 (8) (2017) 1150–1160.
[44] J.D. Hathaway-Schrader, C.M. Novince, Maintaining homeostatic control of periodontal bone tissue, Periodontol 86 (1) (2000) 157–187, 2021.
[45] M.A. Zinnia, A. Khademul Islam, Fenugreek steroidal saponins hinder osteoclastogenic bone resorption by targeting CSF-1R which diminishes the RANKL/OPG ratio, Int. J. Biol. Macromol. 186 (2021) 351–364.
[46] J.M. Kim, C. Lin, Z. Stavre, M.B. Greenblatt, J.H. Shim, Osteoblast-osteoclast communication and bone homeostasis, Cells 9 (9) (2020) 2073.
[47] W.J. Boyle, W.S. Simonet, D.L. Lacey, Osteoclast differentiation and activation, Nature 423 (6937) (2003) 337–342.
[48] S. Eick, W. Pfister, Efficacy of antibiotics against periodontopathogenic bacteria within epithelial cells: an in vitro study, J. Periodontol. 75 (10) (2004) 1327–1334.
[49] J.D. Johnson, R. Chen, P.A. Lenton, G. Zhang, J.E. Hinrichs, J.D. Rudney, Persistence of extracrevicular bacterial reservoirs after treatment of aggressive periodontitis, J. Periodontol. 79 (12) (2008) 2305–2312.
[50] L. Abusleme, A.K. Dupuy, N. Dutzan, N. Silva, J.A. Burleson, L.D. Strausbaugh, J. Gamonal, P.I. Diaz, The subgingival microbiome in health and periodontitis and its relationship with community biomass and inflammation, ISME J. 7 (5) (2013) 1016–1025.
[51] Y. Okabe, R. Medzhitov, Tissue biology perspective on macrophages, Nat. Immunol. 17 (1) (2016) 9–17.
[52] B. Xiao, Levering mechanically activated Piezo channels for potential pharmacological intervention, Annu. Rev. Pharmacol. Toxicol. 60 (2020) 195–218.
[53] L. Wang, X. You, S. Lotinun, L. Zhang, N. Wu, W. Zou, Mechanical sensing protein PIEZO1 regulates bone homeostasis via osteoblast-osteoclast crosstalk, Nat. Commun. 11 (1) (2020) 282.
[54] G. Hajishengallis, Periodontitis: from microbial immune subversion to systemic inflammation, Nat. Rev. Immunol. 15 (1) (2015) 30–44.
[55] F. Moroni, B.J. Dwyer, C. Graham, C. Pass, L. Bailey, L. Ritchie, D. Mitchell, A. Glover, A. Laurie, S. Doig, E. Hargreaves, A.R. Fraser, M.L. Turner, J.D. M. Campbell, N.W.A. McGowan, J. Barry, J.K. Moore, P.C. Hayes, D.J. Leeming, M. J. Nielsen, K. Musa, J.A. Fallowfield, S.J. Forbes, Safety profile of autologous macrophage therapy for liver cirrhosis, Nat. Med. 25 (10) (2019) 1560–1565.
[56] S. Yamanaka, Pluripotent stem cell-based cell therapy-promise and challenges, Cell Stem Cell 27 (4) (2020) 523–531.
[57] Y.L. Zhao, P.X. Tian, F. Han, J. Zheng, X.X. Xia, W.J. Xue, X.M. Ding, C.G. Ding, Comparison of the characteristics of macrophages derived from murine spleen, peritoneal cavity, and bone marrow, J. Zhejiang Univ. - Sci. B 18 (12) (2017) 1055–1063.
[58] S. Depil, P. Duchateau, S.A. Grupp, G. Mufti, L. Poirot, `Off-the-shelf` allogeneic CAR T cells: development and challenges, Nat. Rev. Drug Discov. 19 (3) (2020) 185–199.
[59] J. He, X. Xiong, H. Yang, D. Li, X. Liu, S. Li, S. Liao, S. Chen, X. Wen, K. Yu, L. Fu, X. Dong, K. Zhu, X. Xia, T. Kang, C. Bian, X. Li, H. Liu, P. Ding, X. Zhang, Z. Liu, W. Li, Z. Zuo, P. Zhou, Defined tumor antigen-specific T cells potentiate personalized TCR-T cell therapy and prediction of immunotherapy response, Cell Res. 32 (6) (2022) 530–542.